THE UNIVERSITY OF READING

Department of Mathematics

Using Optimal Estimation Theory for Improved Rainfall Rates from Polarization Radar

BY

GEMMA FURNESS

Supervisor Dr Robin Hogan

August 2005

ACKNOWLEDGEMENTS

CONTENTS

1. INTRODUCTION

Precipitation measurements are one of the main areas of interest and application in radar meteorology. Weather influences many aspects of life and economic value such as crop & livestock farming, wind and hydropower production, effective ground and air transport through to outdoor leisure events. With severe weather occurrences such as storms and flash floods causing some of the most frequent and devastating natural hazards world wide, there is a growing demand for accurate quantitative measurements of rainfall. It has been shown that flooding causes more deaths and damage than any other hydro meteorological phenomenon world wide, and was the 2nd leading cause of weather related deaths in 1992 after lighting. Recent events such as the Boscastle floods in 2004, where 2 inches of rain fell in just 2 hours, or the Pakistani floods in Feb 2005 where 278 people died as a result of one week's torrential rain, have highlighted the importance for better localized weather warnings. The scale and intensity of these weather events is governed by atmospheric processes within the hydrological cycle, the movement of water from the oceans to the atmospheres and back to the oceans, via the land, with both local and more global scale effects such as climate change.

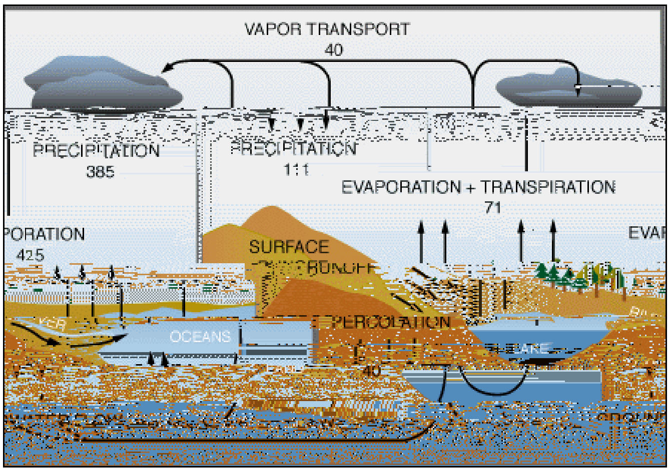

Figure 1. Schematic diagram of the Hydrological cycle (adapted image, original from Scientific American 1989), all units are in $\times 10^{12}$ ^{3} of water transport.

The development of stratiform clouds usually from mid latitudinal frontal systems is g6(s)11y lly slow resulting in smer precipitation drops and light rainfall, wheea s convective structures intensities are being used alongside frequent synoptic observations and NWP mesoscale model data to produce more accurate short range forecasts known as ‘nowcasts’ e.g. in the Met office

1. Introduction

polarization measurements, particularly differential reflectivity at points of azimuth and range

2. RADAR THEORY AND RAIN

Empirical relationships exist relating Z to R using

$$= \quad , \tag{2.3}$$

where Z is proportional to the concentration of drops with fixed diameter D given in Eq.(2.1), hence the return in Z could be equivalent for a high density of small drop as that of fewer larger drops, leading to uncertainties in distinguishing precipitation type. Such relationships have been proposed where rain coefficients and vary, dependant on drop diameter and concentration, giving rise to unique relationships characteristic of different rainfall types.

Z(R) relationship Z= a	Hydrometeor type	Reference
$300\ ^{1.44}$	Spherical ice and water	Rhyde (1946)
$200\ ^{1.6}$	Stratiform rain	Marshall and Palmer (1948)
$31\ ^{1.71}$	Orographic rain at cloud base	Blanchard (1953)
$486\ ^{1.37}$	Thunderstorm rain	Jones (1956)
$140\ ^{1.5}$	Drizzle	Joss et al 1970
$250\ ^{1.5}$	Widespread rain	Joss et al (1970)
$500\ ^{1.5}$	Thunderstorm rain	Joss et al (1970)

Table 1 Empirical Z(R) relationships for varying hydrometeor types, using conventional reflectivity, a measured in $^{6}\ ^{-3}(\quad ^{-1})^{-}$

For a scan of hydrometeor particles with a classified rain type, we can find a set of coefficients (and) which provide the best fit to the Z(R) relationship (see Eq.2.3) allowing R to be estimated, such as those proposed above for drizzle, widespread rain and thunderstorms (by Joss et al 1970), but in reality these coefficients are expected to vary spatially between different rain types even within a single radar scan. Atlas and Ulbrich (1974) have shown that early empirical relationships between radar reflectivity at non-attenuating wave lengths do not account for such different rainfall types, hence conventional reflectivity Z(R) relations based on single-parameter drop size distributions are prone to large errors. Important extensive research has been carried out showing that raindrops under aero-dynamical stress vary with size, becoming increasingly oblate with increased size, but conventional radar are unable to detect these properties. To overcome this problem, reflectivity measurements at both vertical and horizontal polarizations have been introduced to determine both oblateness and size plus drop concentration hence resulting in better rainfall rates.

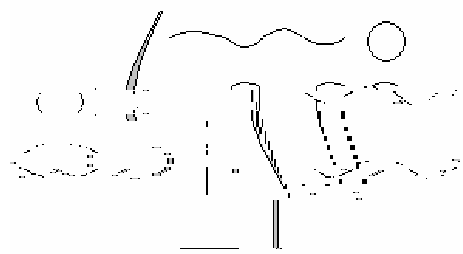

The oblateness of raindrops falling at terminal velocity through the atmosphere is known to increase with drop volume. With such measurements it is possible to relate drop size distributions such as the exponential function proposed by Marshall and Palmer (1948) given by Eq. (2.5)

$$(\quad) = \ {}_0 \exp(-3.67 \quad / \quad {}_0) \quad {}^{-3} \quad {}^{-1}, \tag{2.5}$$

to rainfall rate. Where is the individual drop diameter, ${}_0$ is the median volume drop diameter, ${}_0$ is the concentration parameter fixed by ${}_0$ and the observed value of actual reflectivity

there is little, if any cross polar return in the , yet cells of slightly high polar activity around within the range of -20 to -26 , which can be distinguished from heavy rain fall with an upper band of ≈-26 and lower band of around -34 (Chandrasekhar and Bringi 2001).

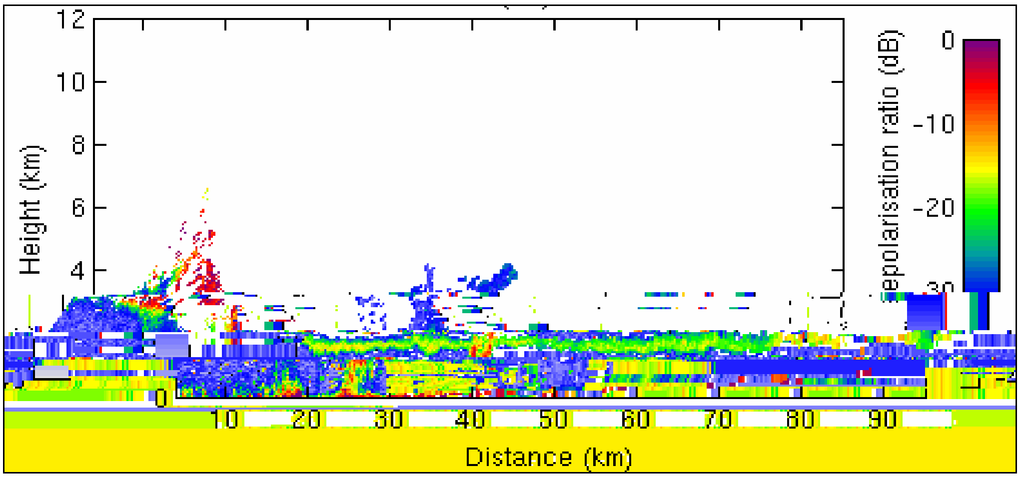

Figure 5 Vertical RHI scan of linear depolarization ratio (dB) equivalent location and time to figures 3 & 4. Showing clear anomalous propagation at low ground levels 0.1 to 0.2km high, and higher –20

Such relationships are also advantageous since they are likely to be unaffected by attenuation inaccuracies, or spurious hail measurements. Inaccuracies can arise since these relationships assume ϕ can be measured to 1° or better, but in reality the ϕ resolutions can be quite noisy, with large perturbations of up to ± 5 ° in some cases. Measuring the velocity gradient rather than return intensity can also result in inaccuraciesi1.6798 241.i3. 11.647 5.2(1(n)-5.8(coccura)-t. Tmin)5.

$$(\quad) = {}_{0} \; {}^{\mu} \exp \frac{-(3.67+\mu)}{{}_{0}} \qquad (0 \le \quad \le {}_{\max}) \tag{2.10}$$

(2.10) is equivalent to that of the exponential DSD proposed by Marshal and Palmer Eq.(2.5) if the spectrum shape parameter μ governing the shape of the distribution is = 0. This new 3-parameter gamma distribution has a range of tuneable parameter sets μ, $_0$ and $_0$ derived by Ulbrich from the range of empirical Z(R) relationships published by Battan (1973). For or a better representation of the variations in drop size distributions Illingworth and Blackman (2002) have shown that a normalized form of Eq.(2.10) where the 3 variables become independent, each representing real physical characteristics is more consistent with DSD observations Eq.(2.11). The natural variability of rain drop size spectra are hence well captured by this normalized 3-parameter gamma distribution

$$(\quad) = \quad (\mu) \left(\frac{}{{}_{0}} \right)^{\mu} \exp \frac{-(3.67+\mu)}{{}_{0}} \quad , \tag{2.11}$$

where

$$(\mu) = 0.033 \frac{(3.67+\mu)^{\mu+4}}{\Gamma(\mu+4)} \;, \tag{2.12}$$

is now the normalized concentration parameter independent of the spectrum width μ.

Such distributions were invented to overcome the non-independence of μ and $_0$ present in

fluctuating instrumental error, leading to unrealistic negative rain rates, hence we combine unconditionally positive Z with polar parameters or for more accurate results.

formulae) relating the observations to the state variables, where $\_ = \mathrm{H}[\_]$ can be used directly for a linear problem. For slightly non-linear problems the forward model can be linearized about some prior state to find a solution, yet many heavily non-linear realistic systems are not adequate for linearization within the desired accuracy of the measurements.

3.2 The least squares method and the non-linear problem

Early inverse modeling techniques proposed by Laplace required perfect and complete input data, but radar data which is often noisy and incomplete lends itself to a another type of inverse problem where a line of best fit can be used as an approximating function, even though it might not agree precisely with the data at any point. Such an approach is the ‘method of least squares’, sometimes called the ‘method of differential correction’ using observations to refine an initial estimate, by minimizing the squared differences between the values on the approximating line and the observed data.

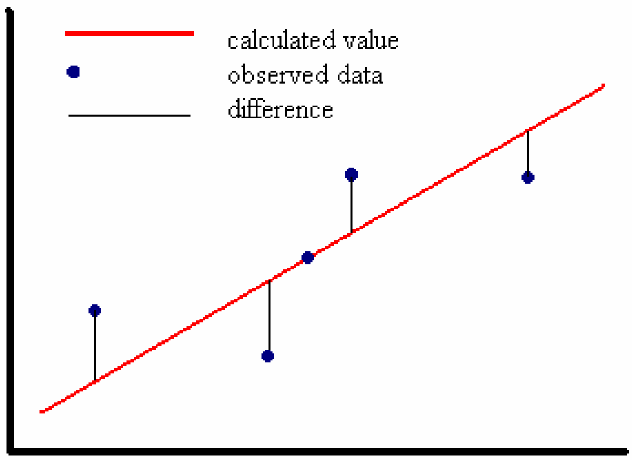

Figure 7 diagramatic representation of the least squares fit or linear regression line for the linear case, where the line of best fit is found my minimizing the sum of the squares of these differences.

Inverse problems can be particularly difficult to treat if there are many unknown parameters or if the forward model is heavily non-linear, especially if no previous knowledge of the parameters are available (R. Bannister 2003). Fortunately our moderately non-linear problem with a relatively low number of parameters and prior information is manageable.

$$[\_] = \frac{1}{2}(\_ - \quad [\_])\ \_^{-1}(\_ - \quad [\_]) \tag{3.2}$$

For simplicity this is equivalent to the first term only of Eq.(3.1), the ‘a priori’ state (second term) has been removed to be re-introduced in section.3.2.2. In general _ is the state vector (size), _ the observation vector (size), is the forward model operating on the observations and _ an $\times$ covariance matrix containing the uncertainty or standard deviations of the observations squared. If the observational errors of different _ components are uncorrelated it follows that _ is diagonal matrix of the variances for each individual element of _. Y

If we substitute Eq. (3.4) into the cost function Eq. (3.2) we have Eq.(3.6)

[__]

$$\delta\_\_ = \_^{-1}\_\_ \ \_^{-1}\delta\_ ,\qquad (3.11)$$

from which we can determine _ using $\_\_ = \delta\_\_ + \_\_{0}$.

It is unlikely that the first minimum of , will predict the best estimate of _ particularly if the initial guess is considerably different to the current state , so this process of linearization and minimizing is then repeated, where the previous value of _ then becomes $\_\_{0}$, about which we linearize. This process is repeated in a Newtonian iteration fashion (Rodgers 2000) where we update our initial guess at each iteration using $\_\_ \rightarrow \_\_{0} + \delta\_\_$, the iterative loop terminates when the values of __and $\_\_{0}$ converge to a chosen suitable degree of accuracy.
This final vector _ giving rise to the minimum value of the cost function $_{min}$ at ∇ = 0 is known as the analysis vector__ . In our problem __ contains the optimal parameters

$$\_ = \_\_ \; \_^{-1} \_\_ + \_^{-1}, \tag{3.13}$$

It then follows that our new extended update matrix $\delta\_\_$ becomes

$$\_\_ \quad \_^{1}\{\_\_ \; \_^{1} \; \_ \quad \_ \quad ^{1}(\_\_ \quad \_\_ \quad)\}$$

such as the ‘cubic spline’ for improving piecewise cubic Lagrange and piecewise cubic Hermite interpolation. Basis splines which we shall denote B-splines from now on, can be linear, quadratic or cubic with the particular property of local control. Bartels et al (1987) have shown that local control makes it possible to alter a single data point to modify only part of a curve or surface without affecting points outside of its vicinity, unlike a polynomial or Fourier transform. The equation for a B-spline of -order with n+1 control points

Rodgers (2000) uses techniques similar to Eq.(3.18) and Eq. (3.19) in his discussion of the Kalman smoother where a best estimate of some quantity is needed from given data for before and after the desired time, the filter is run forwards in time as described, then additionally run backwards, commencing with a prior estimate given by the final analysis of the forward time series. For the scope of our project we will only implement the Kalman smoother in the forward direction.

Simulation of more realistic evolving dynamical systems are commonly described in versatile four-dimensional variation schemes, capturing the complex time and space scales of real physical processes. Lermusiaux and Robinson (1999) discuss further filtering and smoothing schemes via data assimilation for evolving error subspace statistical estimation (ESSE).

4. THE RETRIEVAL ALGORITHM

4.1 Observational data

The observational data for our algorithm provided by the Chilbolton S-band radar UK on 19th May 1999, gives varying scans at elevations from 0.5º dwelling in low level precipitation though to

<u>DATA SET 1</u>: ‘Horizontal Plan-Position Indicator (PPI) radar scan with shallow elevation 0.5º, at time 16:29:18’

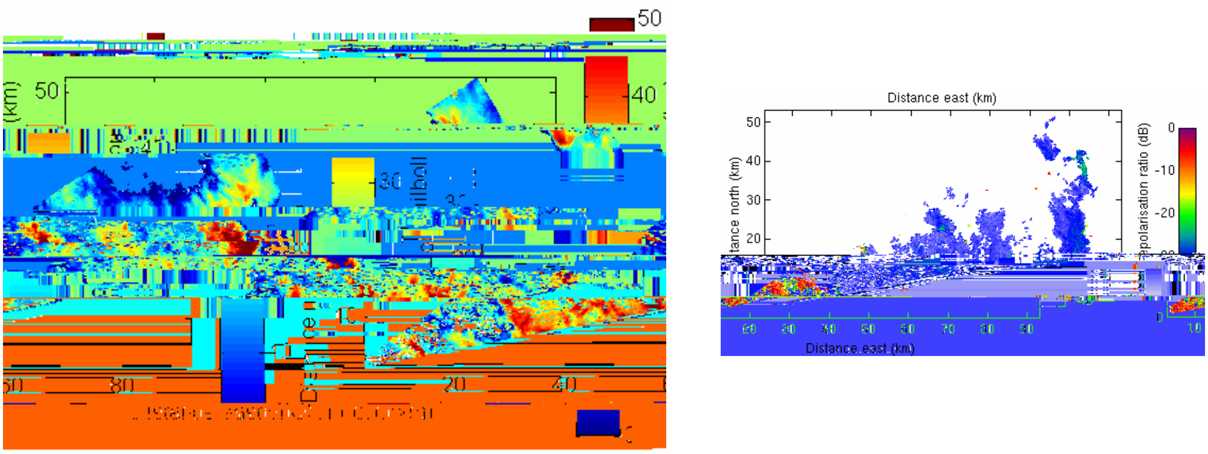

Figure 9 A PPI radar reflectivity scan at elevation 0.5º dwelling in low level precipitation, observed with the narrow S-band Chilbolton radar in the UK on 19th May 1999, at 16:29:28. Data with Spurious linear depolarization returns (>-10) have been removed. Warm coloured areas of high reflectivity visible in the ENE direction.

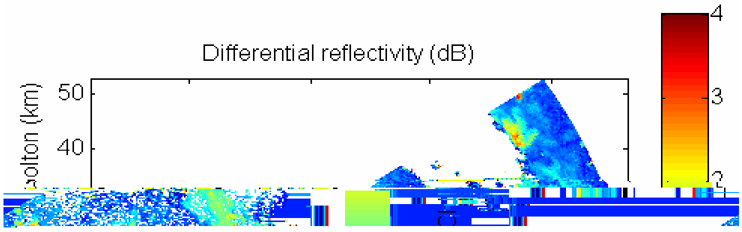

Figure 10 Differential reflectivity cross section at 0.5º, observed with the narrow S-band Chilbolton radar in the UK on 19th May 1999, at equivalent time to Fig. 9. Evidence of oblate drops in returns at various points in range and Azimuth, (>-10 removed).

Visual analysis of the conventional reflectivity field (see Fig.9) and the equivalent polarized reflectivity returns, indicate similarities in the location of precipitation features, with heavy rainfall characteristics identifiable from high ≥ 30 corresponding to ≥ 1 triggered by oblate droplets. Between 60km and 80km east we can see a region of range gates triggering minimal polarized returns of $0 \quad \leq 1$

<u>DATA SET 2</u>: ‘Horizontal (PPI) scan at 2.0º’ elevations, affected by melting layer at mid range, retrieved at 16:38:06.

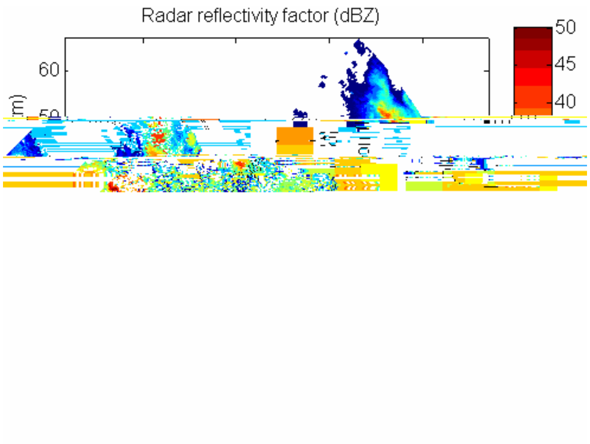

Figure 11 A PPI radar reflectivity scan with higher target elevation 2.0º covering varying levels of precipitation with range, from the S-band Chilbolton radar in the UK on 19th May 1999, at 16:38:06. Data with spurious linear depolarization returns (>-10

RHI SCAN Vertical (Range Height Indicator) profile of the atmospheric state taken at 16:53:46

<u>DATA SET 3:</u> 'Horizontal (PPI) radar data with mid level elevation 0.7º, at time 16:55:33'

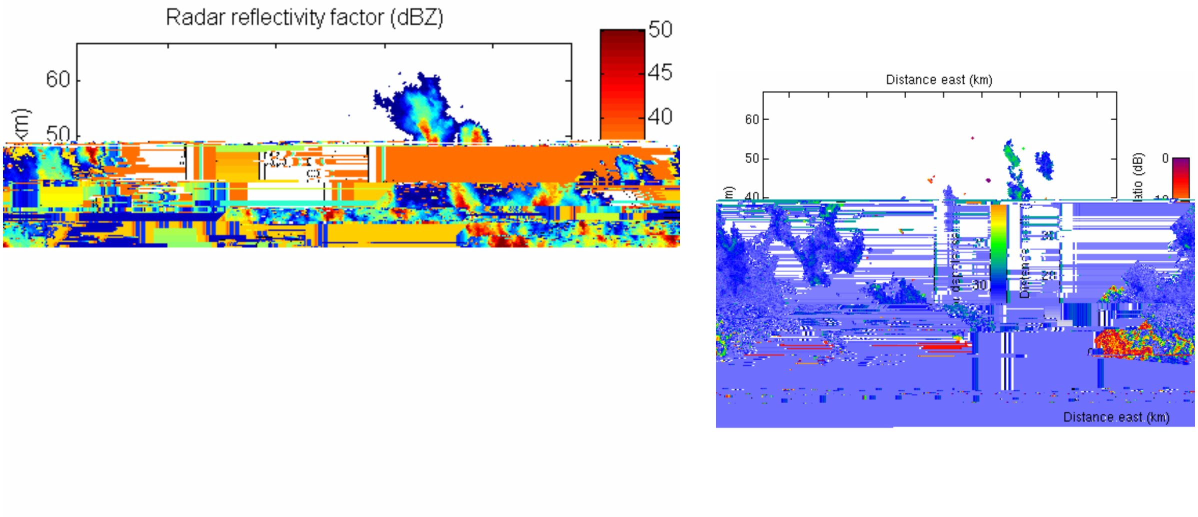

Figure 14 A PPI radar reflectivity scan at elevation 0.7º dwelling in low/mid level precipitation ranging from ground level at close range to just beneath the melting layer at far distance (90km). Observed with the Chilbolton S-band radar on the 19th May 1999,at a later time 16:55:33 (17:27 minutes on from data set 2). Data with Spurious linear depolarization returns (>-10) evident at close range has been removed.

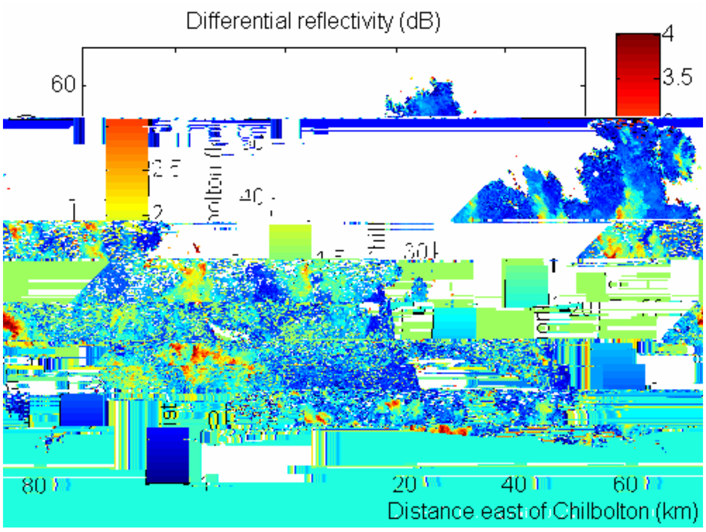

Figure 15 Horizontal profile of differential reflectivity for data at elevation 0.7º, observed with the narrow S-band Chilbolton radar in the UK on 19th May 1999, at 16:55:33 showing evidence of more oblate drops with positive over numerous range gates in range and azimuth, data containing >-10 dB has again been removed.

Observations with negative returns indicating unphysical negative rainfall rates will be ignored in the retrieval scheme when computing R using R(Z,) relationships.

4.2 Methodology

The optimal estimation scheme designed for use on each data set exploits individual measurements of Z, and

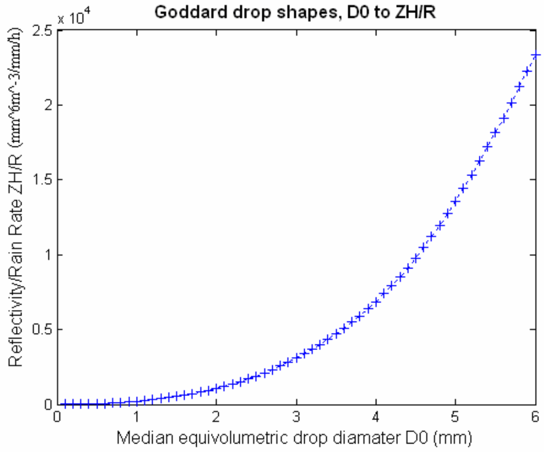
Goddard drop shapes, D0 to ZH/R
x 10^4
2.5
2
1.5
1
0.5
0
0
1
2
3
4
5
6
Reflectivity/Rain Rate ZH/R (mm^6m^-3/mm/h)
Median equivolumetric drop diamater D0 (mm)

Figure 17

METHOD 1: Constant & per ray, no a priori data constraint

If we first consider the case with only an initial guess of the state variables $_0 = (\; , \;)$ with a=200 and b=1.6 (Marshall and Palmer 1948) for each ray (azimuth), we then wish to determine an optimum analysis state $= (\; , \;)$ for each ray from which we can estimate rainfall rate at each pixel using Eq.(4.4). Each ray in the north easterly domain will be processed in turn commencing with the most northerly finishing at the most easterly ray. There will be no relation between adjacent rays at this stage.

Our Jacobian _ Eq.(4.1) using both Eq.(4.7) and Eq.(4.8) will be an $\times 2$ matrix where is the number of finite and elements within the full range of each ray. It then follows that the Hessian matrix as described in Section (3.2) Eq.(3.10) $\_ = \_ \; \_^{-1} \_ = (\; \times 2) \; (\; \times \;)(\; \times 2)$ is an invertible 2×2 0.5j4T88893 Tm000e986.6433 0 0 11.61Tj160.1.4(0.6234 108 Tw88893 T10/T(3.)5. Fi T

The variances in the a priori constraints ln( ) and will be taken to be 0.5 and 0.002 respectively, allowing error variations of ln( ) ± 0.71 equivalent to $98.6 \leq \quad \leq 405.6$ $^{6} \; ^{-3}(\quad ^{-1})^{-}$ and errors in of ± 0.045.

The Hessian $\_ = \_\_ \; \_^{-1} \_\_ + \_ \; ^{-1} = (2\times2) + (2\times2)$ remains a square 2×2 matrix, and the update vector $\delta\_\_ = \_^{-1}\{\_\_ \; \_^{-1}\delta\_ - \_ \; ^{-1}(\_\_ - \_\_ \;)\} = (2\times2)^{-1}\{(2\times1) - (2\times2)(2\times1)\}$ is again a 2×1 vector containing δ and δ as in method 1. At this stage of the retrieval algorithm and have been constrained by a realistic prior state, but do not best represent the physical fluctuation state within each ray, hence we will introduce a method to overcome this.

<u>METHOD 3: Constant and calculated over ranges of length 3km or 9 km, within each ray.</u>

We then use a similar approach to that of Thompson and Illingworth (2003) to calculate an independent analysis state vector for numerous range gates within each ray of total length ≈ 90 km, rather than the continuity of method 2. We subdivide each ray into n sections, in our case using n=10 (equivalent to 9km) or 30 sections (length 3km) and apply the retrieval algorithm to optimize the unique state of each section. For each ray the state vector $\_\_ = (\_,\_)$ now has n components of both and , again with the initial guess $_0$ equal to a=200 and b=1.6. Our Jacobian Eq.(4.1) is now a $\times 2$ matrix given by

(   ) (   )

$$(\ \times\ ) = \tag{4.12}$$

We then calculate Jacobian_hat denoted $\hat{\_}$, the derivative of each measurement of with respect to each component of $\hat{\_} = (\hat{\_}, \hat{\_})$ giving an $\times 2$ matrix, which is a quasi-diagonal matrix containing the change in each observation of with its equivalent state parameters and denoted on each diagonal.

$$\frac{\partial}{\partial\ \hat{}\ (\theta\varphi)}, \frac{\partial}{\partial \hat{}} = \begin{pmatrix} \partial/\partial\hat{} & 0 & 0 \\ 0 & & 0 \\ 0 & 0 & \partial/\partial\hat{} \end{pmatrix}, \begin{pmatrix} \partial/\partial\hat{} & 0 & 0 \\ 0 & & 0 \\ 0 & 0 & \partial/\partial\hat{} \end{pmatrix}$$

variables and . To compute this Jacobian it is necessary to multiply each side of $\hat{\_}$ by the weighting function W, to give the desired function

$$= \frac{\partial}{\partial \ \hat{}} \times \ , \frac{\partial}{\partial \hat{}} \times \ = \frac{\partial}{\partial}, \frac{\partial}{\partial} \tag{4.14}$$

$$\begin{aligned} &= [(\ \times \ )(\ \times \ ), (\ \times \ )(\ \times \ )] \\ &= [(\ \times \ ), (\ \times \ )] \\ &= (\ \times 2 \ ). \end{aligned}$$

The Hessian and update then follow from method 3. A final, smoother $\times 2$ analysis state vector $\hat{\_} = \left(\ln(\hat{\_}), \hat{\_}\right)$ can be calculated from the final $\times 2$ analysis state $\_ = (\ln(\_), \_)$, from which we can then calculate $= \ / \hat{} \ ^{1/\hat{}}$ to give a more accurate estimate of rainfall at each pixel.

<u>METHOD 5</u>: ‘additional continuity constraint in azimuth using the Kalman smoother approach’

The finale step in developing the most accurate retrieval system is to implement a Kalman filtering technique Eq.(3.19) for a smoother relation from ray to ray. To do this we introduce an additional weighted constraint using the final analysis state from the previous estimate at time t-1 denoted , taken to be the most recent computed state of the adjacent ray. We will implement the Kalman smoother in the forward direction, from most Northerly to East, but in future work an additional smoothing in the opposite direction could be tested. The Hessian function now with the

The update state (Eq.4.16) now contains __ = (_, _)

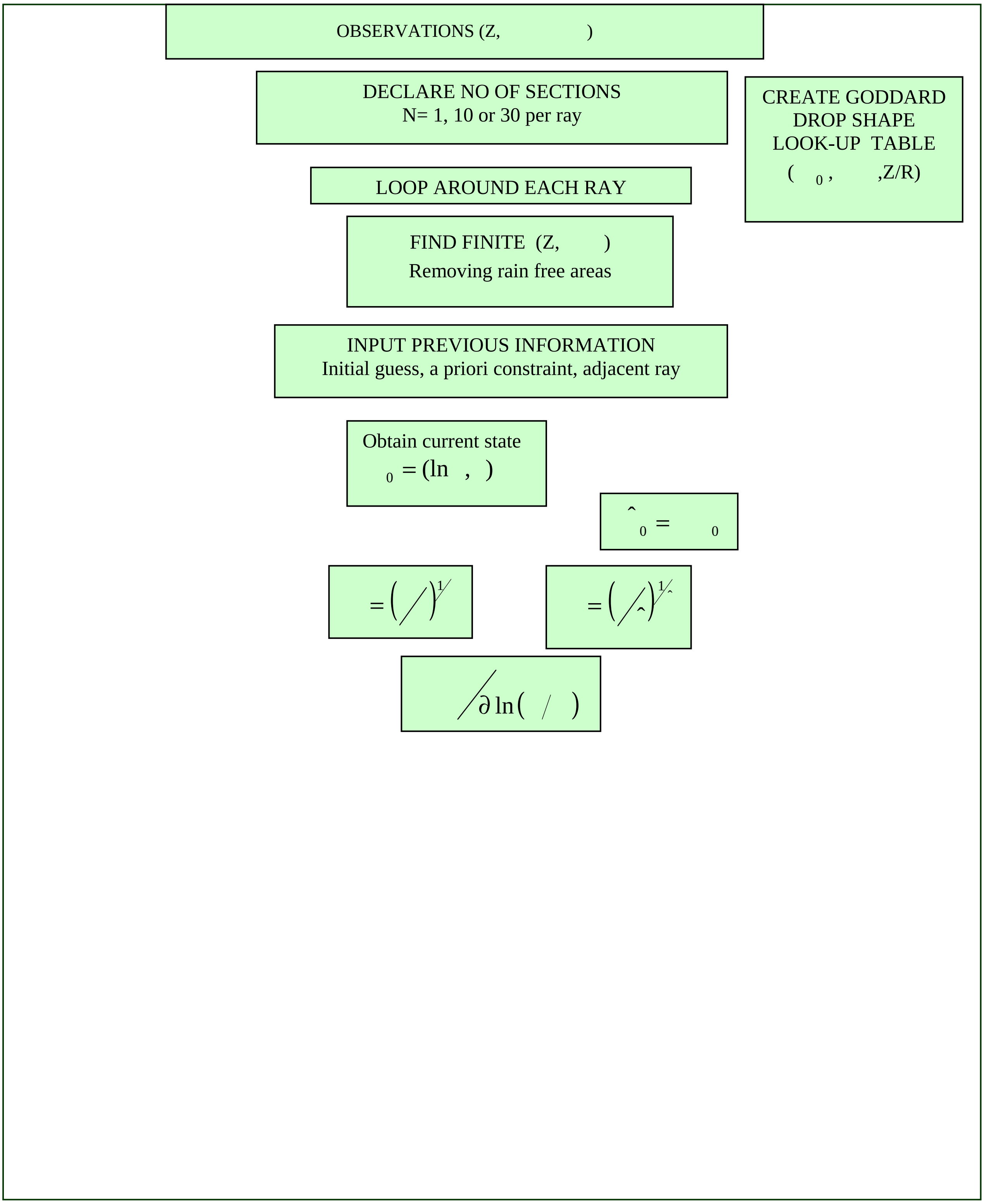

Figure 19 Flow diagram showing the each stage of the retrieval algorithm, the red line for the weighted spline of method 4, and the Newtonian iteration of the forward model represented by the blue line loop. i) simple forward model, ii) converts basis function weights into state variables, iii) forward model to obtain from Z/R.

We now implement method 2 on the observed (Z,) field to calculate a single Z(R) relationship for each ray, with an initial guess and a priori constraint both equivalent to a=200 and b=1.6.

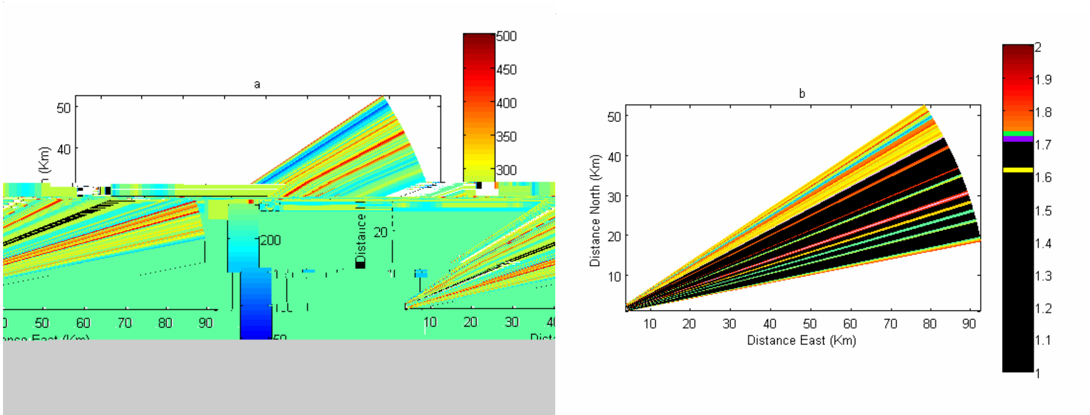

Figure 23 plots of state variables _ _ _ calculated for each ray in azimuth, where visibly higher values of constant

In the log difference profile Fig.(24) 3dB and -3dB represent a difference factor in the final rain

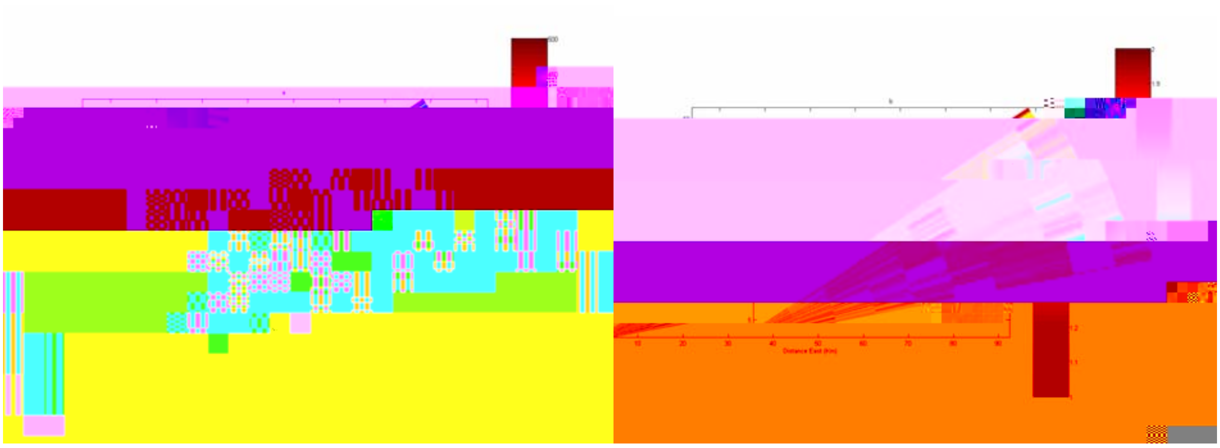

Figure 26 State variables _ _ _ calculated for each ray over every 3km in range, showing large fluctuations in the state parameters for each ray.

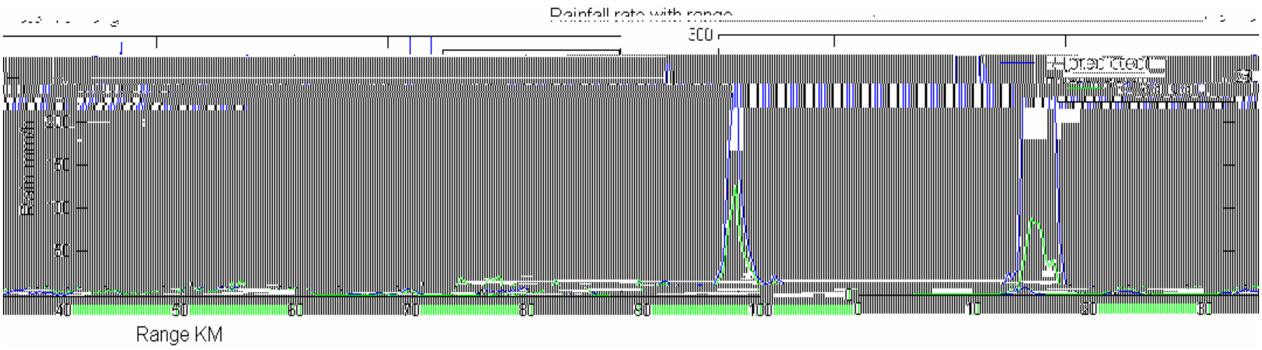

Figure 27 Rain rate for the equivalent easterly ray of (Fig.25) where the estimated rain rate peaks with conventional reflectivity (57km, and 83km). For $55 \leq \quad \leq 63$ we have a=346 and b=1.27, and for $82 \leq \quad \leq 90$ a=25.78 b-1.42, different relationships both giving rise to increased rain estimates.

Figure 27 shows the sensitivity of the combination of and in the Z(R) relationship Eq.(4.4) in predicting rain from reflectivity intensity. The same set of state coefficients can produce either higher or lower estimates of rain than the standard state (a=200, b=1.6) predictions, dependant on the measured reflectivity Z ( ). Essentially a low value of does not necessarily infer high rain rate unless it is combined with a low coefficient, nor does a high value of always imply low rain rates. Using the analysis state _ (_,_) and but at a more dense drop concentration indicated by high Z, hence resulting in heavier rain rates in the model forecast.

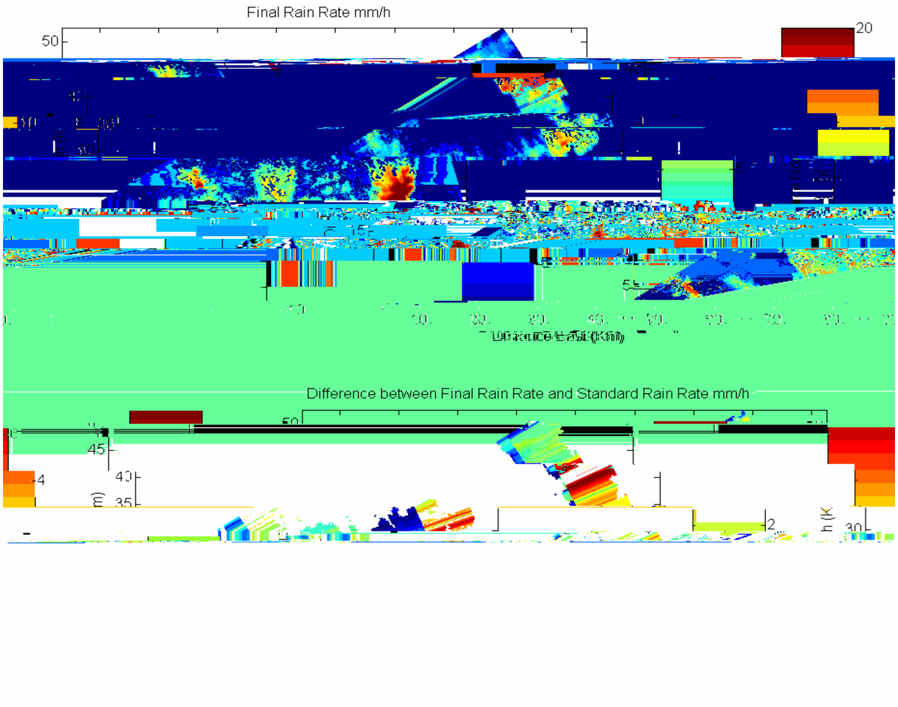

Figure 28 Plot in logarithmic units ( ) of the final rainfall rate $^{-1}$, with 10 sets of state coefficients for each ray, and the difference between this block-wise estimate state (method 3) and the standard Z(R) state (difference of 6 factor of 4).

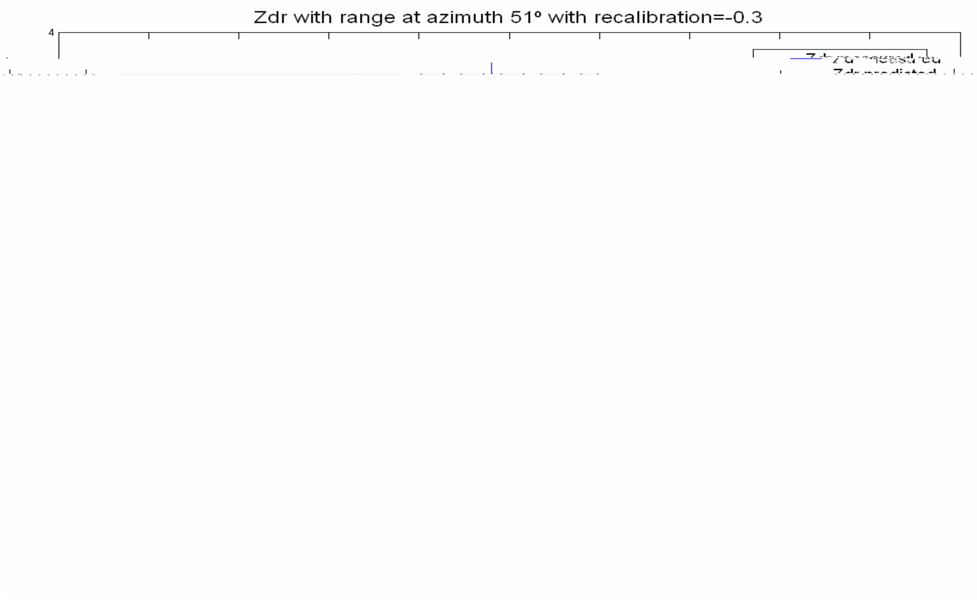

Figure 29 Measured, model estimated and the standard Z(R) differential reflectivity taken from the middle ray of the scan spatially equivalent to Fig.(21). The model is predicted from the constant set of state variables Fig.(26) over every 9km range gate using only a priori data.

If we compare Fig.21 and Fig.29 we can clearly see that the block-wise range techniques of method 3 allows our model to better represent the characteristic highs and lows of the field for finite non-negative observations than the results of method 2, which assume a constant analysis state over the whole domain of each ray.

In analysis of Fig.(28) the ratio between predicted rain rate for the regional approach and the standard rain rate estimates, shows that there are visible areas of sharp variations at regional

The final rainfall rates calculated using the smoothed set of analysis state variable ˆ and ˆ for each individual radar pixel of Fig.(31) shows a vast difference from the standard estimates. An example of thisnc35(b)Ru65 thisnc35ta state of adjacent rays. The results of the optimization enforcing the Kalman smoothing constarint gives smoother state variables (Fig.32) which are then transferred into rain rate (Fig.33).

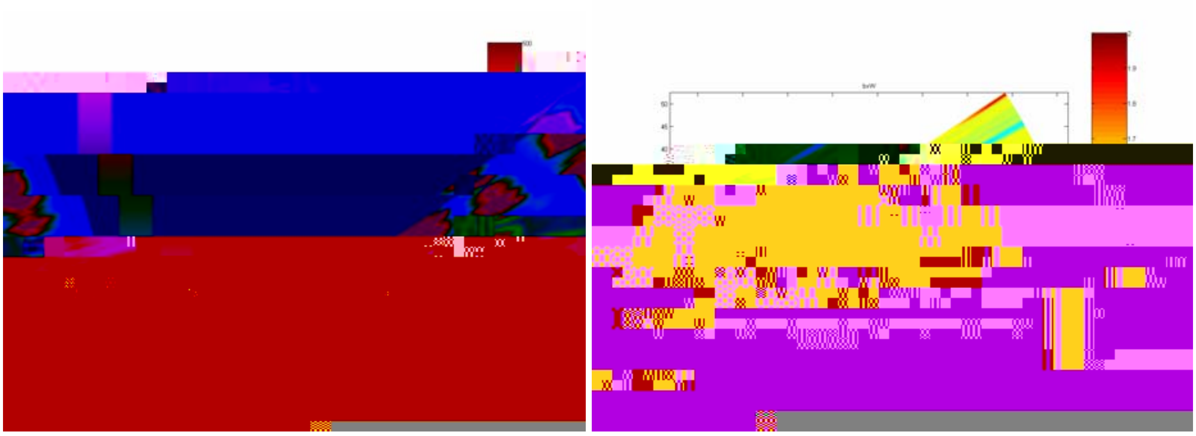

Figure 32 All smooth state variables $\hat{\ } = (\hat{\ }, \hat{\ })$ calculated for each ray with n=10 range sectors within m observations in range, using the weighted linear (m x n) B-spline technique of method 4 and the Kalman filter of method.5 with ray to ray covariance of Eq.(4.17).

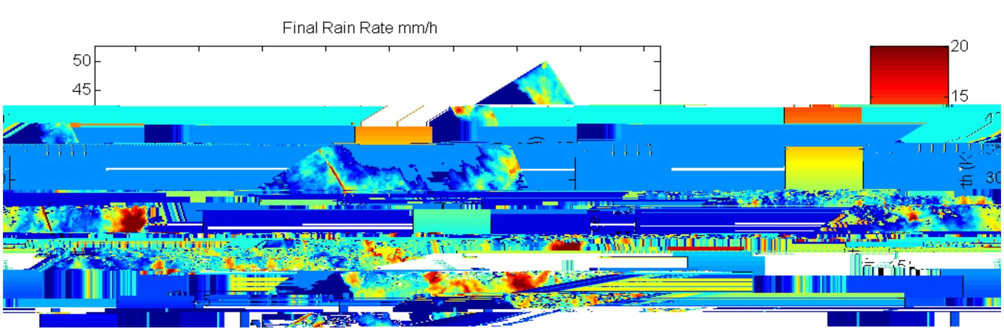

Figure 33 Plot of logarithmic final rainfall rate $^{-1}$ and difference (dB), calculated from

var(lna)=0.5 varb=0.001 for Eq.(4.9), plus the weighted spline function, the results confirm this spatial relation where the characteristic physical features of the simple block-wise process in Fig.(28) remain, becoming even more pronounced with continuity forcing.

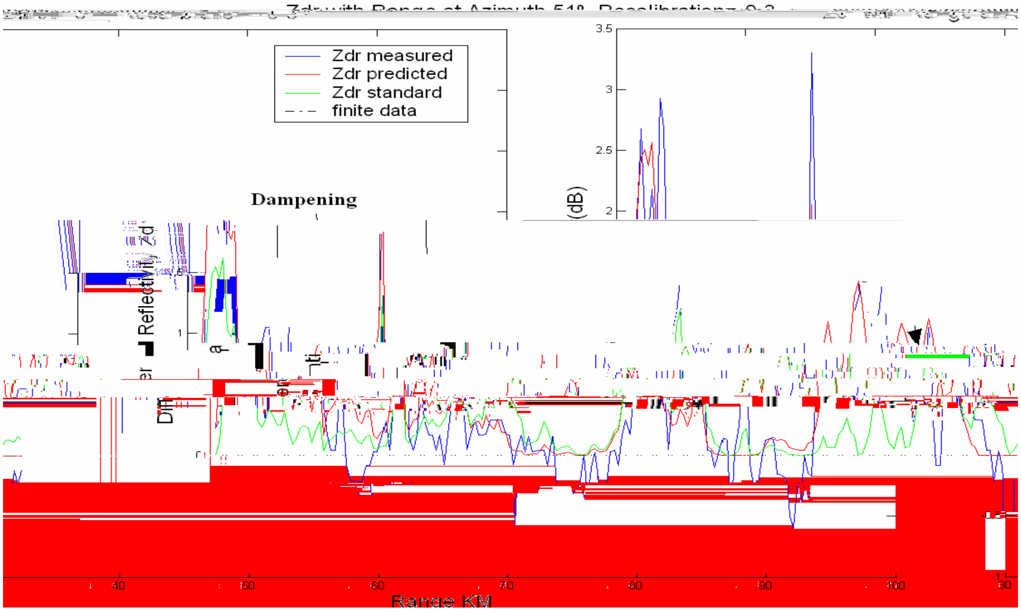

Figure 34 verification by comparing the model, measured and standard differential reflectivity using methods 4 and 5 combined (azim 51º), for range > 30km.

The field predicted using our fully developed model Fig.(34) still shows a more accurate fit to

5.2 Case 2: Choosing regional range lengths for a high elevation scan (2.0º), affected by hail and bright band

Next we will consider the case at 16:38:06 with elevation of 2.0º on 19th may 1999 using data set 2, with 225 measurements in azimuth and 300 within 90km range from the polarized reflectivity fields of Fig.11, Fig.12. Again we re-calibrate the observed by the ‘zero ’ criterion for finite, positive values noting that at 2.0º we expect returns of $-1 \leq \quad \leq 0$ beyond 50km (the melting layer) due to ice, which is clearly visible in the field (Fig.11)

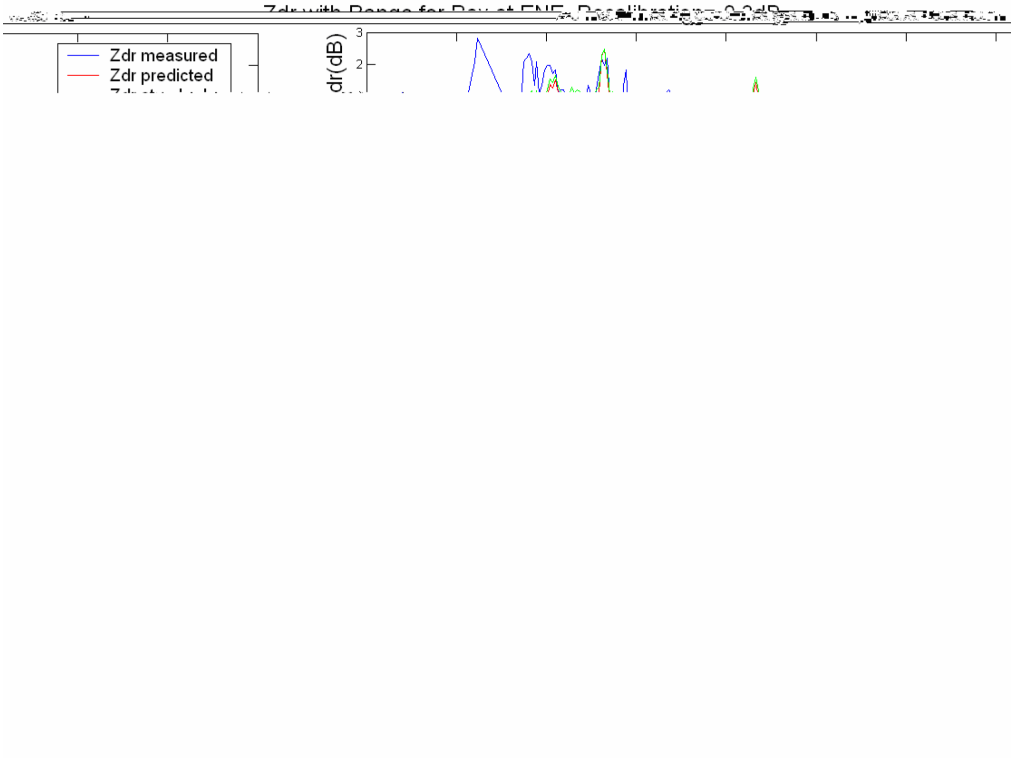

Figure 35 Polarized differential reflectivity (dB) taken at an ENE ray for finite data (recalibration criterion applied to data < 50km) with the equivalent conventional reflectivity field , with high returns (dB) yet falling at further range beyond the melting layer.

Figure 35 shows how polarization returns of low (-1 to 0) at 45km or beyond 50km with very high observations of Z can be used to identify tumbling highly oblate ice particles. Below the melting layer such returns can be the results of extreme concentrations of spherical drops, or more probably an area of hail, Or at higher elevations (2.0º) as the radar signal passes through the melting layer at mid-range in to a region of ice as shown in (Fig.9). We will now optimize the full scan using our smoothed retrieval algorithm, using various regional range lengths.

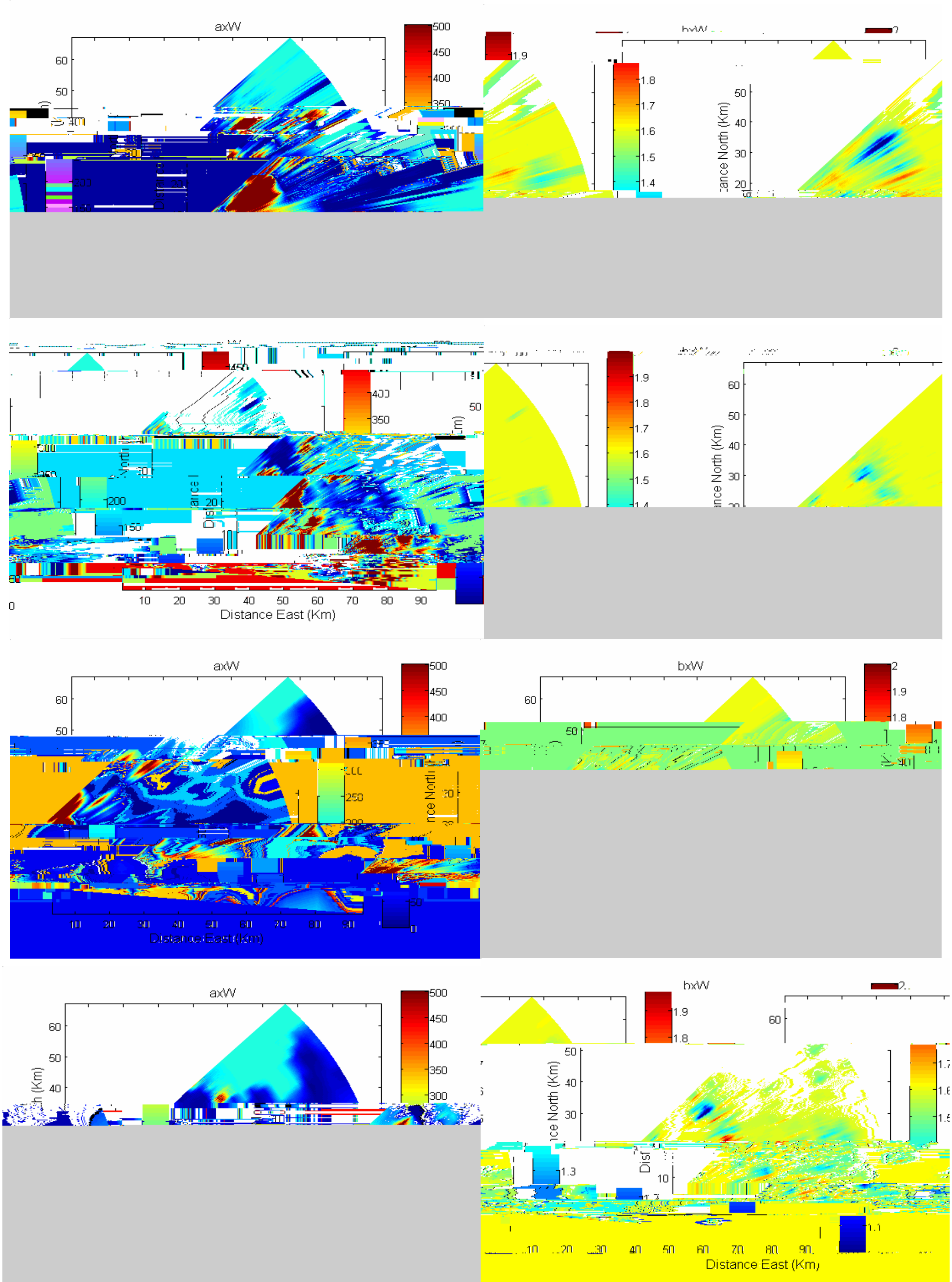

Figure 36 Smooth state variables ˆ_ = (ˆ, ˆ_) for method 4 B-spline with 10 (9km) range sections then 30 (3km) regions, followed by the combined B-spline and Kalman smoothing technique of method 5 for the equivalent range lengths.

For a 2^{o} elevation scan changes in precipitation structure will occur at sharper gradients in range below melting layer than those of a low elevation scan dwelling in precipitation e.g. (Case 1). For this data set such changes may be more accurately represented by implementing more frequent range divisions, for example at every 3km rain gate. The results of the state parameters $\hat{} = (\hat{}, \hat{})$ are shown for the block-wise technique with B-spline weighting and then Kalman smoother for both 3km and 9km region lengths shown in Fig.(36).

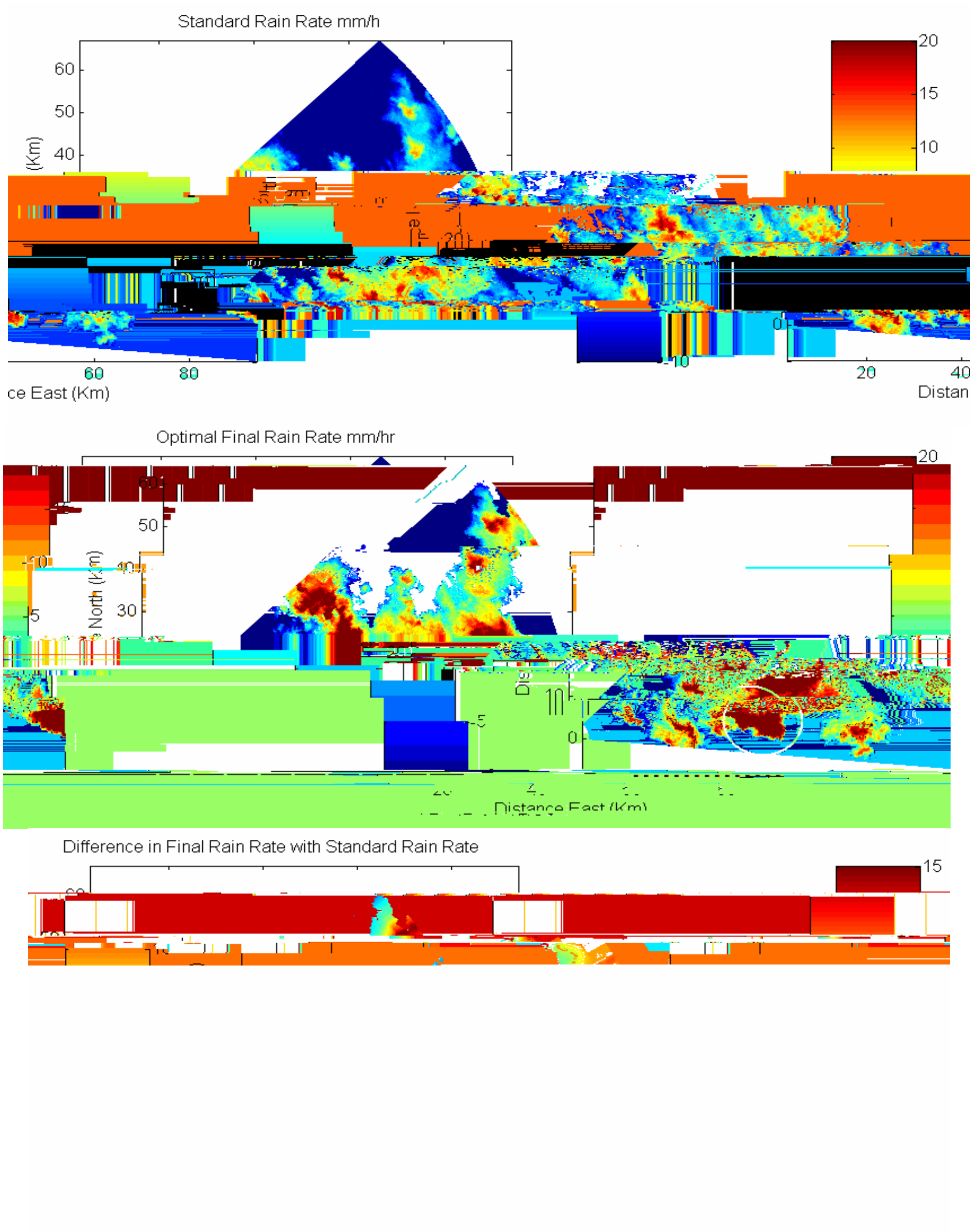

Figure 37 Plots of Standard Rainfall rate ( ) with a=200 b= 1.6, the optimal final rainfall rate using smoothing in azimuth and range, and their logarithmic difference profile with 10 9km sections per ray.

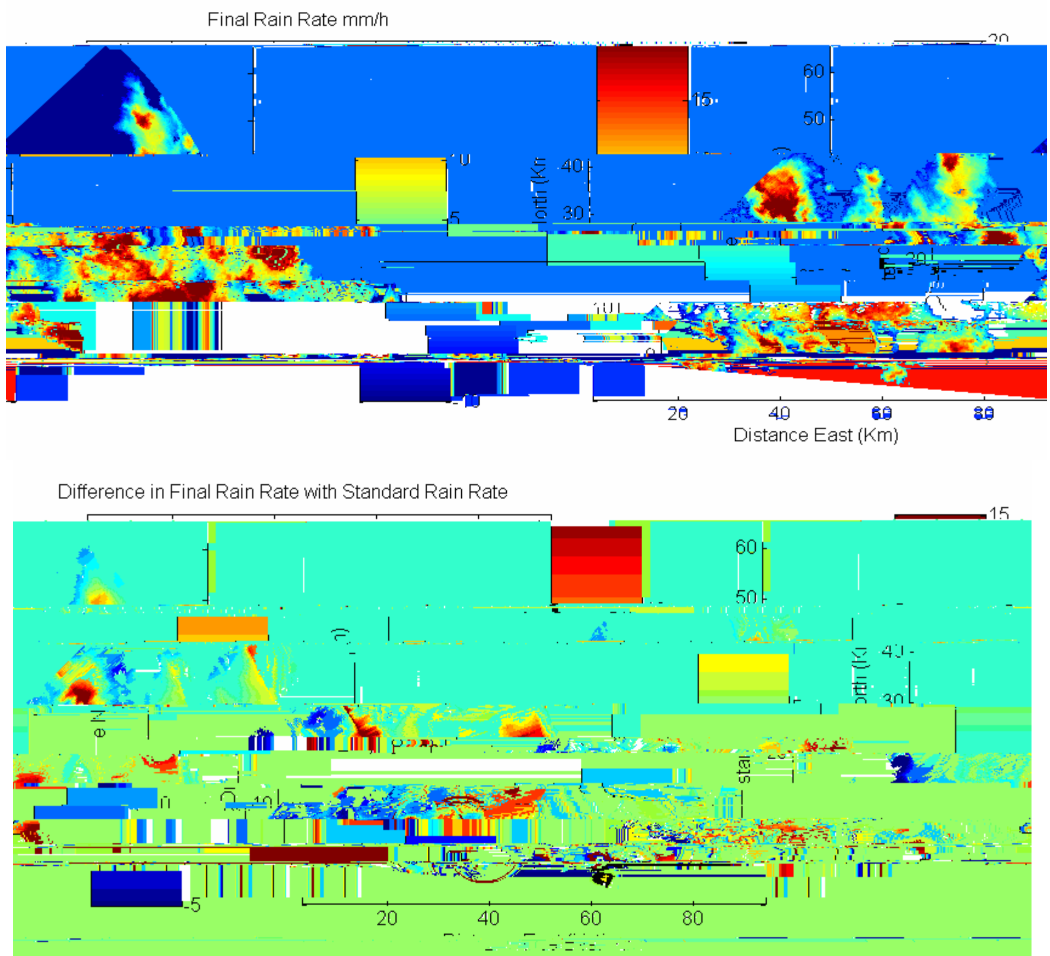

Figure.38. Final rain rate and the difference between them using Eq. (4.18), all in logarithmic units (dB) using the B-spline in azimuth and Kalman smoother in range over 3km range divisions

The final rainfall profiles using the optimal retrieval algorithm over both 3km and 9km range sections seem to strongly agree in the location of precipitation characteristics with only slight variations in rainfall intensity over each area. At 9km (Fig.37) rainfall features above bright band are more intense than those using 3km (Fig.38) shown by larger areas of high R(final)/R(standard) difference ratios ≈15dB in (Fig.37). Below the melting layer logarithmic differences are higher using 3km regions implying better sensitivity to fluctuations at steeper gradients. In each case a major feature resulting in increased rain rate is indicated around 40km to 47km east and 0km to 10km north with a difference factor of up to 15 to previous standard rain estimates, this area coincides with large Z and zero

this area is likely to be underestimated by the conventional model for the standard Z(R) relationship, hence we implement our optimal algorithm using the block-wise smoothed approach.

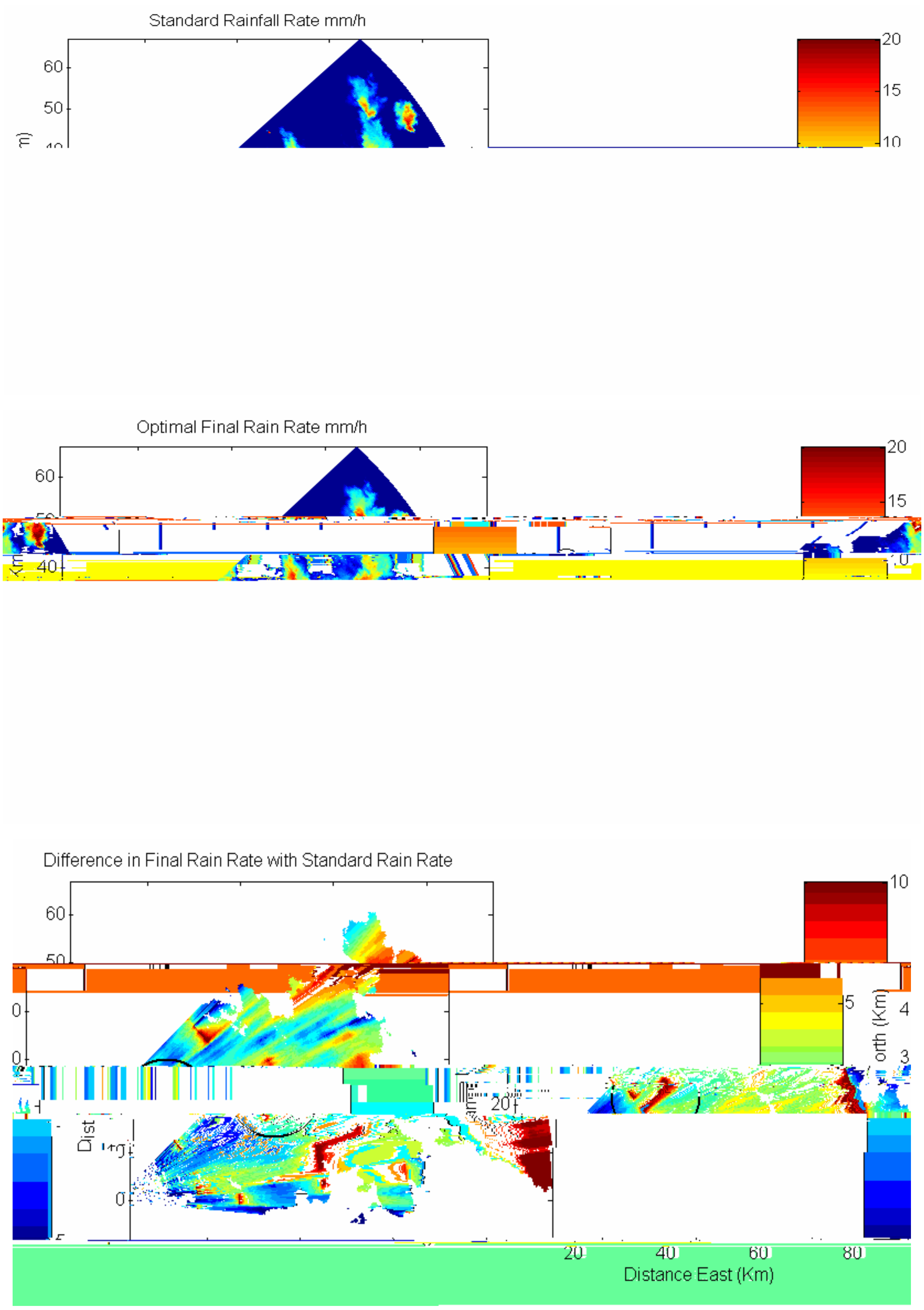

Figure 41 plots of Standard Rainfall rate using mm/hr in logarithmic units (dB) using the standard rainfall coefficients a=200 b= 1.6, the optimal final rainfall rate using the smoothed state in azimuth and range of Fig.(42), and their logarithmic difference profile Eq.4.(18). Region of heavy rain high with Z, and indicated.

The rain rate predictions surrounding the returns of returns at (A) and (C) in (Fig.40) predict heavier rainfall levels using the block-wise approach than that of the standard model as expected, clearly visible in the circled region of logarithmic difference profile around 30km NNE. But this area of heavy attenuating rainfall is may have affected the stability of the retrieval algorithm at rain gates beyond this range, hence other polarization parameters could be applied gate by gate to correct for attenuation (Smyth and Illingworth 1998). The retrieval algorithm using the original ray to ray correlation covariance as proposed in method 5 using the covariance matrix Eq.(4.17) predicts the rain rates of Fig.(41) which are given by optimized state variables shown by Fig.(42).

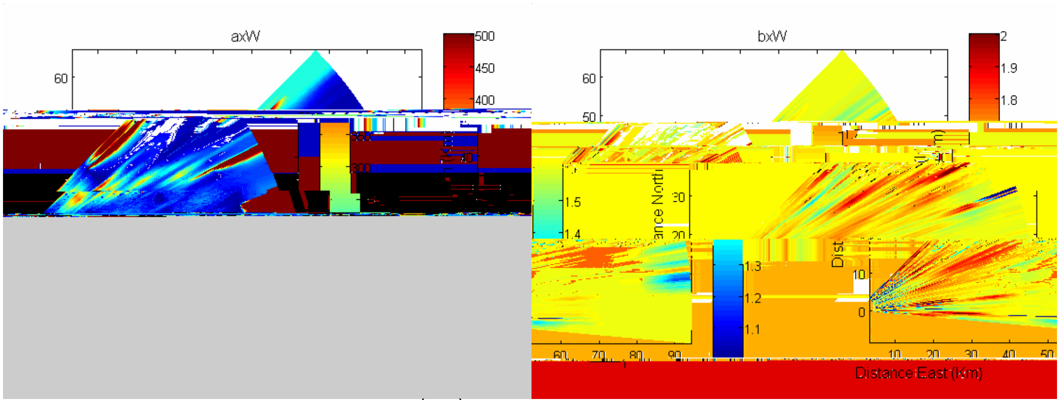

Figure 42 Plot of all smooth state variables $\hat{\_} = (\hat{\ },\hat{\ })$ calculated for each pixel using optimization with 10 range gates, the linear B-spline (method 4) and the forward Kalman smoother of (method 5).

Using the current smoothing constraints Fig.(41) we can still see sharp edges at ray boundaries in the state variable field, implying that a tighter relation in azimuth could be enforced. To increase this ray to ray correlation such that our co-variance matrix represents stronger spatial continuity we use $\mathrm{var}\ln(\ \ ) = 0.02$ and $\mathrm{var}(\ \ ) = 0.009$ equivalent to ± 0.03 and ± 0.14 error deviations respectively, the results of this are shown in Fig.(43).

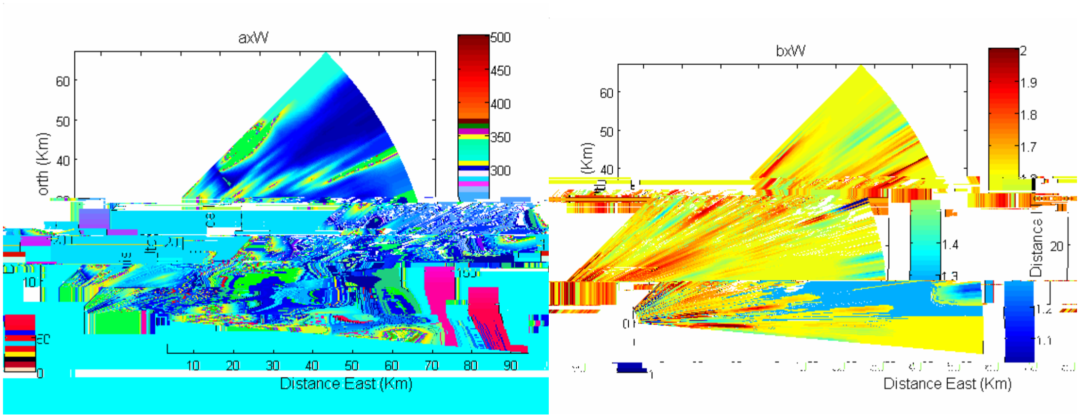

Figure 43 Smooth state variables $\hat{\ }$ and $\hat{\ }$ using the optimization of methods 4 and 5, but with a stronger ray to ray relation in the Kalman smoother, $\mathrm{var}\ln(\ \ ) = 0.02$ error of ± 0.14 and $\mathrm{var}(\ \ ) = 0.0009$ or ± 0.03 error Eq. (4.17).

features and hence under-estimate rain rates, so we will subsequently assume the original constraint of $\mathrm{var}\ln(\quad) = 0.03$ and $\mathrm{var}(\quad) = 0.001$ for improved rain estimates in the optimal model.

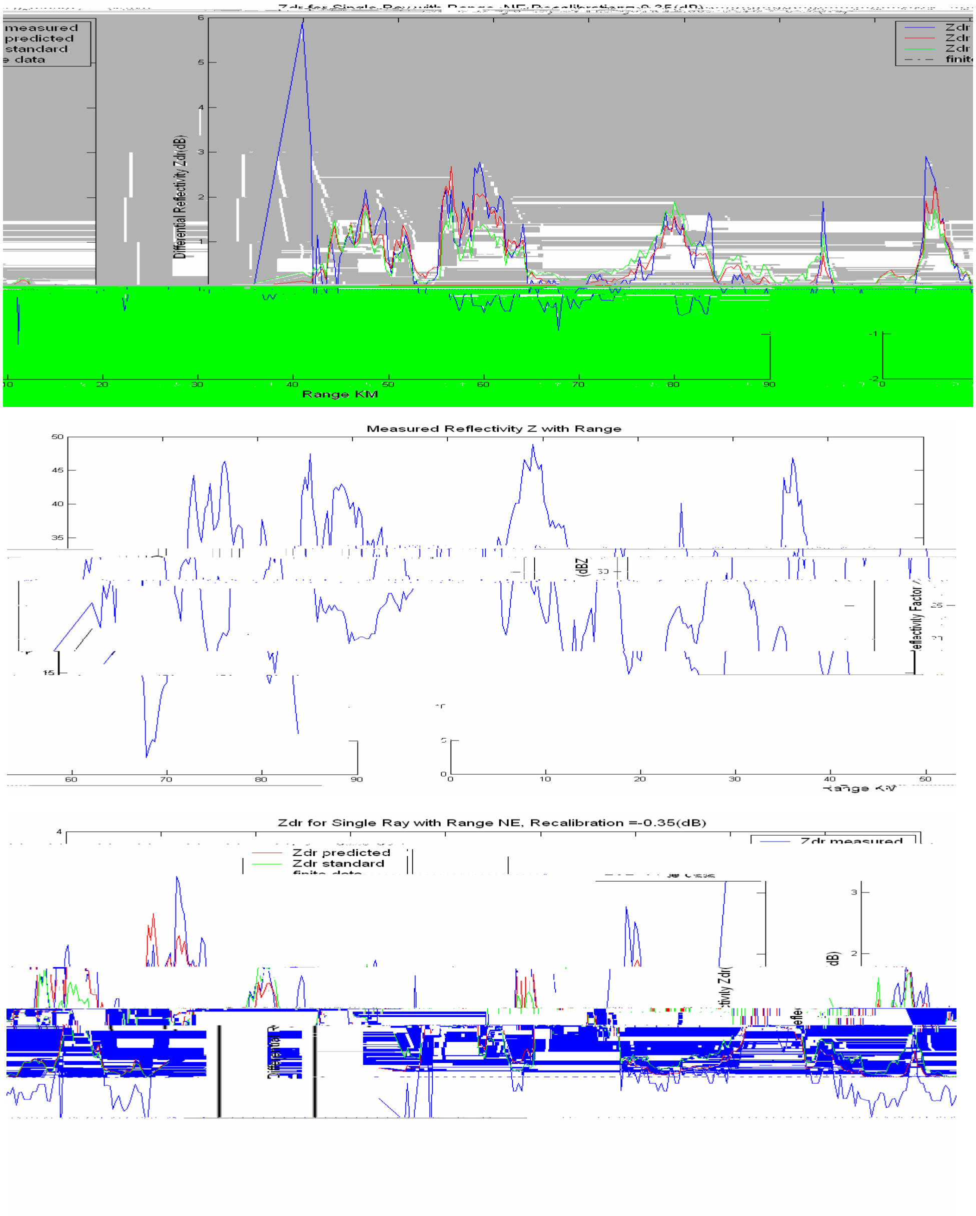

Figure 45 Plot to compare final predicted, measured and standard differential reflectivity using methods 4 and 5 combined over two adjacent rays in the NE direction. The upper plot showing the most northerly profile, and the lower its adjacent more easterly ray of . Reflectivity field Z for the more northerly ray.

The model predictions shown in Fig.(45) show a better fit to the measured data than the predictions

6 CONCLUSIONS

6.1 Analysis and model evaluation

This study has emphasized the important role of combining conventional and polarization radar data (particularly Z and) to provide essential drop diameter and concentration information required for more accurate rainfall rate estimates using block-wise optimal estimation theory techniques. The method of least squares has proved to be a powerful tool in performing a region by region optimization, using the (Marshall and Palmer 1948) prior state for stratiform rain and the widely used normalized gamma distribution of raindrop size spectra Eq.(2.11), for fixed $\mu = 5$ drop shapes of Goddard et al (19995). Exploiting such raindrop information we propose an optimal retrieval algorithm for determining a set of state variables $= (\, , \,)$ per region or smoothed state $\hat{} = (\hat{}, \hat{})$ with continuity in range and/or azimuth at each range gate to infer unique Z(R) relationships Eq.(2.3), alternative to the ideal but costly gate by gate / approach similar to that of Thompson and Illingworth (2003).

Our model uses the assumptions that Z (dBZ) should scale with R $^{-1}$ for a given rain drop diameter ($_0$) and hence , with natural variations in the normalized drop concentration represented in the formula / = ( ). Commencing with an initial guess and back ground state we use Z(R) relationships to calculate rain rate and hence development the results in the analysis state and hence rain rate without enforced smoothness showed encouraging signs of spatial continuity, but occasional unphysical sharp variations between regional boundaries suggested the need for stronger gate to gate relation. Linear 1-D B-splines were implemented to smooth unphysical discontinuities in range, then the concept of the Kalman smoother applied to constrain the relation of the ray to ray analysis. These techniques generally showed confirmation of the already apparent physical gate to gate similarities within a radar scan, by enhancing the influence of evident physical features in resulting precipitation

6.2 Future work

The determination of rain fall rates from using Z and alone in the operational environment can lead to major errors where heavy rain can attenuate the radar beam. This could be accounted for in the retrieval algorithm using calculations of differential attenuation (–) (functions of Z/R) to perform a gate by gate correction scheme along a ray on the polarization measurements and such that differential reflectivity can then be calculated properly using Eq.(2.4) and hence improve rain rate validity. Smyth and Illingworth (1998) propose a similar approach using additional polarization measurements and ϕ to ensure a numerically stable attenuation correction algorithm.

The results of our smoothing techniques show definite improvements in range gate relation, yet the Kalman smoother did not give show the same level of filtering, without over dampening results. Better use of the Kalman smoother could be implemented by performing the smoothing procedure ray to ray in both the forward and backward direction (see Sect.3.2.2), requiring the problem to be reformulated to operate on the whole region. A more obvious suggestion would be to implement a 2-D Basis to smooth in both range and azimuth fo

7. REFERENCES

ATLAS, D. & ULBRICH, C. W. (1974): ‘The physical basis for attenuation-rainfall relationships and the measurement of rainfall parameter by combined attenuation and radar methods’, J. Rech. Atmos, **8**, 275-298.

BANNISTER, R. (2003): ‘The method of least squares used to invert an orbit problem’. Amer. J. Phys, **71**(12), 1268-1275.

BARTELS, R. H., BEALTY, J. C. & BARSKY, B. A. (1987): ‘An introduction to splines for use in computer graphics and geometric modeling’.

BATTAN, L. J. (1973): ‘Radar Observations of the Atmosphere’, University of Chicago Press, Chicago.

BLANCHARD, D. C. (1953): ‘Raindrop size distribution in Hawaiian rains’, J. Met, **10**, 457-473.

BRINGI, V. N. & CHANDRASEKAR, V. (2001): ‘Polarimetric Doppler weather radar, principles and applications’. CUP, pp 636.

CHANDRASEKAR, V., BRINGI, V. N., BALAKRISHNAN, N. & ZRINIC, D. S. (1990): ‘Error structure of multiparameter radar and surface measurement of rainfall. Part III: Specific differential phase’. J. Atmos. Oceanic Technol., **7**, 621-629.

COLLIER, C.G. (1991): ‘NIMROD-A system for nowcasting and initialization for modelling using regional observational data’, Preprints,25th Int. Conf. on Radar Met.,24-28 June, Paris, France, Am. Met. Soc. Boston, pp.21-24.

ILLINGWORTH, A. J. & BLACKMAN, T. M. (2002): ‘The need to represent raindrop size spectra as normalized cTf1. Met. Soc. B. Met TeN, cago( )-5. CUalc.f(i)-0.5(-2.3(c.th n)-4.947 25)]TJerp ’.

RODGERS, C. D. (2000): ‘Inverse methods for atmospheric sounding, theory and practice’. World Sci., River edge, NJ.

SACHIDANANDA, M. & ZRNIĆ, D. S. (1987): ‘Rain rate estimates from differential polarization measurements’. J. Atmos. Oceanic Technol, **4**, 588-598.

SELIGA, T. A. & BRINGI, V. N. (1976): ‘Potential use of radar differential reflectivity